NUMERICAL ANALYSIS OF LOW REYNOLDS NUMBER FLOWS AROUND THIN WINGS FOR MICRO AIR VEHICLES

Yang Aiming* Ni Yunhua Weng Peifen*****

Shanghai Institute of Applied Mathematics and Mechanics, Shanghai University, Shanghai 200072, China

Keywords: ***low Reynolds number, MAV, low-aspect-ratio wings, artificial compressibility method***

Abstract

The low Reynolds number aerodynamics of low-aspect-ratio wings for Micro Air Vehicles applications was numerically investigated. The viscous flows around MAVs wings with different aspect ratio (0.5, 1 and 2) were simulated by solving incompressible Navier-Stokes equations. The hyperbolic equations were formulated by artificial compressibility method with the convective terms discreted using a third-order upwind scheme based on Roe's approximate Riemann solver. The equations were solved using an implicit line-relaxation method with Baldwin-Barth one-equation turbulence model. Numerical results for a thin-flat wing agreed well with the experiment data. The influence of aspect ratio and camber was analyzed in detail. Further results showed the different flow structures for those wings with different camber.

1 Introduction

Micro aerial vehicles (MAVs) are of great interests to both military and civilian applications. The basic characters of MAVs can be described as: maximum dimension of 6 inches or less; flight speed of 10~20m/s; mass of about 10~100 grams; cruising range of several kilometers or more with a mission duration of 20 to 60 minutes. Owing to their small scale, low weight and low cost, MAVs are superior to conventional aircraft in some special conditions where small vehicles is needed.

According to the type of lift generation, MAVs can be divided into three kinds: fixed-wing MAVs; flapping-wing MAVs; rotary-wing MAVs. In this paper, we investigated the fixed-wing MAVs aerodynamic performance to which not many people paid attention in the past. In fact, the Reynolds number of fixed-wing MAVs flow is about 10^5. This Reynolds number is unfamiliar for the aeronautical scientists because it wasn't encountered in conventional aircraft design. In addition, the aspect ratio of MAVs wing is as low as 0.5~2.0 for the scale limit. The low Reynolds number flow around such low aspect ratio wings attracted much less attention.

In this paper, the low Reynolds number aerodynamic property of low-aspect-ratio wings for MAVs applications was numerically investigated. This analysis will provide the aerodynamic design of fixed-wing MAVs with essential theoretic foundation. By solving the Reynolds-averaged incompressibleNavier-Stokes

This project was supported by NSFC grant 10272073

* Associate Professor, Shanghai Institute of Applied Mathematics and Mechanics , Shanghai University, amyang@mail.shu.edu.cn
** Graduate student, Shanghai Institute of Applied Mathematics and Mechanics , Shanghai University, yunhua_ni@hotmail.com
*** Professor, Shanghai Institute of Applied Mathematics and Mechanics , Shanghai University, pfweng@mail.shu.edu.cn

equations using artificial compressibility method [1,2,3], low Reynolds number flows around low-aspect-ratio wings was simulated. To get high viscous resolution, the convective terms time discretization scheme was implicit, and the resulting block heptad-diagonal matrix equation was solved using Gauss-Seidel line relaxation method which has a good convergence behavior. The turbulence model used here is Baldwin-Barth one-equation turbulence model[4].

2 Governing Equations

To couple the pressure and velocity fields, a time derivative of pressure is added to the continuity equation, resulting in

$$\frac{\partial p}{\partial \tau} + \beta \nabla \bullet \vec{q} = 0 \qquad (1)$$

where β is the pseudo-compressibility constant, τ is the pseudo-time variable. Also, a pseudo-time derivative of velocity is added to the momentum equations to get hyperbolic-parabolic equations. So the resulting momentum equations are

$$\frac{\partial \vec{q}}{\partial \tau} + (\vec{q} \bullet \nabla)\vec{q} = -\frac{1}{\rho}\nabla p + \upsilon \nabla^2 \vec{q} \qquad (2)$$

The steady-state solutions of Eq.(1) and (2) with respect to pseudo-time is steady-state incompressible physical solutions.

The complete governing equations written in generalized curvilinear coordinates are given by

$$\frac{\partial}{\partial \tau}\hat{D} + \frac{\partial}{\partial \xi}\left(\hat{E} - \hat{E}_v\right) + \frac{\partial}{\partial \eta}\left(\hat{F} - \hat{F}_v\right) + \frac{\partial}{\partial \zeta}\left(\hat{G} - \hat{G}_v\right) = 0 \qquad (3)$$

where

$$\hat{D} = \frac{1}{J}\begin{pmatrix} p \\ u \\ v \\ w \end{pmatrix} \quad \hat{E} = \frac{1}{J}\begin{pmatrix} \beta U \\ uU + p\xi_x \\ vU + p\xi_y \\ wU + p\xi_z \end{pmatrix} \quad \hat{F} = \frac{1}{J}\begin{pmatrix} \beta V \\ uV + p\eta_x \\ vV + p\eta_y \\ wV + p\eta_z \end{pmatrix}$$

were discreted in space using a third-order upwind scheme based on Roe's approximate Riemann solver.

$$\hat{G} = \frac{1}{J}\begin{pmatrix} \beta W \\ uW + p\zeta_x \\ vW + p\zeta_y \\ wW + p\zeta_z \end{pmatrix}$$

$$U = \xi_x u + \xi_y v + \xi_z w \qquad V = \eta_x u + \eta_y v + \eta_z w$$

$$W = \zeta_x u + \zeta_y v + \zeta_z w$$

$$\hat{E}_v = \frac{\upsilon_e}{J}\begin{pmatrix} 0 \\ (\nabla\xi \bullet \nabla\xi)u_\xi + (\nabla\xi \bullet \nabla\eta)u_\eta + (\nabla\xi \bullet \nabla\zeta)u_\zeta \\ (\nabla\xi \bullet \nabla\xi)v_\xi + (\nabla\xi \bullet \nabla\eta)v_\eta + (\nabla\xi \bullet \nabla\zeta)v_\zeta \\ (\nabla\xi \bullet \nabla\xi)w_\xi + (\nabla\xi \bullet \nabla\eta)w_\eta + (\nabla\xi \bullet \nabla\zeta)w_\zeta \end{pmatrix}$$

$$\hat{F}_v = \frac{\upsilon_e}{J}\begin{pmatrix} 0 \\ (\nabla\eta \bullet \nabla\xi)u_\xi + (\nabla\eta \bullet \nabla\eta)u_\eta + (\nabla\eta \bullet \nabla\zeta)u_\zeta \\ (\nabla\eta \bullet \nabla\xi)v_\xi + (\nabla\eta \bullet \nabla\eta)v_\eta + (\nabla\eta \bullet \nabla\zeta)v_\zeta \\ (\nabla\eta \bullet \nabla\xi)w_\xi + (\nabla\eta \bullet \nabla\eta)w_\eta + (\nabla\eta \bullet \nabla\zeta)w_\zeta \end{pmatrix}$$

$$\hat{G}_v = \frac{\upsilon_e}{J}\begin{pmatrix} 0 \\ (\nabla\zeta \bullet \nabla\xi)u_\xi + (\nabla\zeta \bullet \nabla\eta)u_\eta + (\nabla\zeta \bullet \nabla\zeta)u_\zeta \\ (\nabla\zeta \bullet \nabla\xi)v_\xi + (\nabla\zeta \bullet \nabla\eta)v_\eta + (\nabla\zeta \bullet \nabla\zeta)v_\zeta \\ (\nabla\zeta \bullet \nabla\xi)w_\xi + (\nabla\zeta \bullet \nabla\eta)w_\eta + (\nabla\zeta \bullet \nabla\zeta)w_\zeta \end{pmatrix}$$

$$J = \left|\frac{\partial(\xi,\eta,\zeta)}{\partial(x,y,z)}\right| \qquad J^{-1} = \left|\frac{\partial(x,y,z)}{\partial(\xi,\eta,\zeta)}\right|$$

In the above, (u,v,w) are the velocity components in cartesian coordinates, and υ_e represents a sum of the kinematic viscosity and the turbulent eddy viscosity, that is

$$\upsilon_e = \frac{\upsilon_l + \upsilon_t}{q_0 L_0}$$

where υ_l is the kinematic viscosity, υ_t is the turbulent eddy viscosity.

3 Implicit scheme

Residual vector is defined as

$$\hat{R} = \frac{\partial}{\partial \xi}(\hat{E} - \hat{E}_v) + \frac{\partial}{\partial \eta}(\hat{F} - \hat{F}_v) + \frac{\partial}{\partial \zeta}(\hat{G} - \hat{G}_v)$$

The pseudo-time derivative is approximated by an implicit Euler finite-difference formula giving

$$\frac{\hat{D}^{m+1}-\hat{D}^{m}}{\Delta\tau}=-\hat{R}^{m+1}$$

where the superscript m denotes quantities at the m-th pseudo-time iteration level. The right hand of the above equation is linearized resulting in

$$\left[\frac{1}{\Delta\tau}I+\left(\frac{\partial\hat{R}}{\partial\hat{D}}\right)^{m}\right]\Delta\hat{D}^{m}=-\hat{R}^{m} \qquad (4)$$

where I is a 4×4 identity matrix.

4 Space discretization

The derivative of the convective flux in the ξ direction is approximated by

$$\frac{\partial\hat{E}}{\partial\xi}\approx\frac{\hat{E}_{j+1/2}-\hat{E}_{j-1/2}}{\Delta\xi} \qquad \frac{\partial\hat{E}_{v}}{\partial\xi}\approx\frac{\left(\hat{E}_{v}\right)_{j+1/2}-\left(\hat{E}_{v}\right)_{j-1/2}}{\Delta\xi}$$

Where $\hat{E}_{j+1/2}$ is a numerical flux and j is the discrete spatial index for the ξ direction.

The viscosity term is approximated using central difference scheme, that is

$$\left(\hat{E}_{v}\right)_{j+1/2}=\frac{1}{2}\left[\left(\hat{E}_{v}\right)_{j+1}+\left(\hat{E}_{v}\right)_{j}\right]$$

The convective term $\hat{E}_{j+1/2}$ is computed using an upwind scheme based on Roe's approximate Riemann solver, that is

$$\hat{E}_{j+1/2}=\frac{1}{2}\left[\hat{E}\left(D_{j+1}\right)+\hat{E}\left(D_{j}\right)-\phi_{j+1/2}\right]$$

The $\phi_{j+1/2}$ is a dissipation term. A first-order upwind scheme is given by

$$\phi_{j+1/2}=\Delta E^{+}_{j+1/2}-\Delta E^{-}_{j+1/2} \qquad (5)$$

where $\Delta E^{+}_{j+1/2}$ and $\Delta E^{-}_{j+1/2}$ are the flux difference across positive or negative traveling waves. The flux difference is computed as

$$\Delta E^{\pm}_{j+1/2}=A^{\pm}(\overline{D})\Delta D_{j+1/2}$$

where the Δ operator is defined as

$$\Delta D_{j+1/2}=D_{j+1}-D_{j}$$

The Roe average $\overline{D}$ is given by

$$\overline{D}=\frac{1}{2}(D_{j+1}+D_{j})$$

The plus (minus) Jacobian matrix has only positive (negative) eigenvalues and is computed from

$$A^{\pm}=X\Lambda^{\pm}X^{-1}$$

$$\Lambda^{\pm}=\frac{1}{2}(\Lambda\pm|\Lambda|)$$

High order accurate approximation may be derived using reasonable combination of flux differences. A third order upwind flux is defined by[3]

$$\phi_{j+1/2}=-\frac{1}{3}\left[\Delta E^{+}_{j-1/2}-\Delta E^{+}_{j+1/2}+\Delta E^{-}_{j+1/2}-\Delta E^{-}_{j+3/2}\right] \qquad (6)$$

5 Evaluation of discrete equations

For simplicity, the residual vector $\hat{R}$ on left hand side of Eq.(4) is approximated with first order accuracy, namely, the dissipation term is expressed by Eq.(5); while the residual vector $\hat{R}$ on right hand side is approximated with higher order accuracy, namely, the dissipation term is expressed by Eq.(6). The residual vector in implicit part is given by

$$\begin{aligned}\hat{R}_{i,j,k}=&\frac{\hat{E}_{j+1/2}-\hat{E}_{j-1/2}}{\Delta\xi}+\frac{\hat{F}_{k+1/2}-\hat{F}_{k-1/2}}{\Delta\eta}\\&+\frac{\hat{G}_{l+1/2}-\hat{G}_{l-1/2}}{\Delta\zeta}-\frac{\left(\hat{E}_{v}\right)_{j+1/2}-\left(\hat{E}_{v}\right)_{j-1/2}}{\Delta\xi}\\&-\frac{\left(\hat{F}_{v}\right)_{k+1/2}-\left(\hat{F}_{v}\right)_{k-1/2}}{\Delta\eta}-\frac{\left(\hat{G}_{v}\right)_{k+1/2}-\left(\hat{G}_{v}\right)_{k-1/2}}{\Delta\zeta}\end{aligned} \qquad (7)$$

The left hand side of the resulting equations will be constructed as following

$$
\begin{aligned}
LHS &= \frac{\hat{D}_{j,k,l}^{m+1} - \hat{D}_{j,k,l}^{m}}{\Delta\tau} \\
&+ \left(\frac{\partial \hat{R}_{j,k,l}}{\partial \hat{D}_{j,k,l-1}}\right)^m \Delta\hat{D}_{j,k,l-1} + \left(\frac{\partial \hat{R}_{j,k,l}}{\partial \hat{D}_{j,k,l+1}}\right)^m \Delta\hat{D}_{j,k,l+1} \\
&+ \left(\frac{\partial \hat{R}_{j,k,l}}{\partial \hat{D}_{j,k-1,l}}\right)^m \Delta\hat{D}_{j,k-1,l} + \left(\frac{\partial \hat{R}_{j,k,l}}{\partial \hat{D}_{j,k+1,l}}\right)^m \Delta\hat{D}_{j,k+1,l} \\
&+ \left(\frac{\partial \hat{R}_{j,k,l}}{\partial \hat{D}_{j-1,k,l}}\right)^m \Delta\hat{D}_{j-1,k,l} + \left(\frac{\partial \hat{R}_{j,k,l}}{\partial \hat{D}_{j+1,k,l}}\right)^m \Delta\hat{D}_{j+1,k,l} \\
&+ \left(\frac{\partial \hat{R}_{j,k,l}}{\partial \hat{D}_{j,k,l}}\right)^m \Delta\hat{D}_{j,k,l}
\end{aligned} \tag{8}
$$

To express the resulting equations in the form of matrix, we should convert the three-dimensional index (j,k,l) into a one-dimensional index n. The two index definitions are related by

$$n = j + (k-1) * j_{\max} + (l-1) * j_{\max} * k_{\max}$$

$$\hat{D}_{j,k,l} = \hat{D}_n$$

Note that

$$N_{o,p,q} = \left(\frac{\partial \hat{R}_{j,k,l}}{\partial \hat{D}_{o,p,q}}\right)^m$$

then Eq.(4) can be written by

$$
B\begin{bmatrix} N_{j,k,l-1}, 0, ..., 0, N_{j,k-1,l}, 0, ..., 0, N_{j-1,k,l}, N_{j,k,l} \\ +\frac{1}{\Delta\tau} I, N_{j+1,k,l}, 0, ..., 0, N_{j,k+1,l}, 0, ..., 0, N_{j,k,l+1} \end{bmatrix} \Delta\hat{D} = -\hat{R} \tag{9}
$$

where B[*] is a block heptad-diagonal matrix, and

$$\Delta\hat{D} = \left[\Delta\hat{D}_1, \Delta\hat{D}_2, ..., \Delta\hat{D}_{j_{\max} * k_{\max} * l_{\max}}\right]^T$$

$$\hat{R} = \left[\hat{R}_1, \hat{R}_2, ..., \hat{R}_{j_{\max} * k_{\max} * l_{\max}}\right]^T$$

For simplicity, grid is assumed to be orthogonal when computing Jacobian matrix of viscosity term, then

$$
\hat{E}_v = \frac{\upsilon_e}{J}\begin{pmatrix} 0 \\ (\nabla\xi \bullet \nabla\xi)u_\xi \\ (\nabla\xi \bullet \nabla\xi)v_\xi \\ (\nabla\xi \bullet \nabla\xi)w_\xi \end{pmatrix} = \frac{\upsilon_e}{J}(\nabla\xi \bullet \nabla\xi) I_m \frac{\partial \hat{D}}{\partial \xi}
$$

$$
\hat{F}_v = \frac{\upsilon_e}{J}\begin{pmatrix} 0 \\ (\nabla\eta \bullet \nabla\eta)u_\eta \\ (\nabla\eta \bullet \nabla\eta)v_\eta \\ (\nabla\eta \bullet \nabla\eta)w_\eta \end{pmatrix} = \frac{\upsilon_e}{J}(\nabla\eta \bullet \nabla\eta) I_m \frac{\partial \hat{D}}{\partial \eta}
$$

$$
\hat{G}_v = \frac{\upsilon_e}{J}\begin{pmatrix} 0 \\ (\nabla\zeta \bullet \nabla\zeta)u_\zeta \\ (\nabla\zeta \bullet \nabla\zeta)v_\zeta \\ (\nabla\zeta \bullet \nabla\zeta)w_\zeta \end{pmatrix} = \frac{\upsilon_e}{J}(\nabla\zeta \bullet \nabla\zeta) I_m \frac{\partial \hat{D}}{\partial \zeta}
$$

Where

$$
I_m = \begin{bmatrix} 0 & 0 & 0 & 0 \\ 0 & 1 & 0 & 0 \\ 0 & 0 & 1 & 0 \\ 0 & 0 & 0 & 1 \end{bmatrix}
$$

For example, in ξ direction, the viscosity term in implicit part is given by

$$
\begin{aligned}
\left(\frac{\partial \hat{E}_v}{\partial \hat{D}}\Delta\hat{D}\right)_{j+\frac{1}{2}} &= \left(\frac{\upsilon_e}{J}\right)_{j+\frac{1}{2}} (\nabla\xi \bullet \nabla\xi)_{j+\frac{1}{2}} I_m \begin{bmatrix} \frac{\partial\left(\hat{D}_{j+1} - \hat{D}_j\right)}{\partial \hat{D}_{j+1}}\Delta\hat{D}_{j+1} \\ +\frac{\partial\left(\hat{D}_{j+1} - \hat{D}_j\right)}{\partial \hat{D}_j}\Delta\hat{D}_j \end{bmatrix} \\
&= \left(\frac{\upsilon_e}{J}\right)_{j+\frac{1}{2}} (\nabla\xi \bullet \nabla\xi)_{j+\frac{1}{2}} I_m \left(\Delta\hat{D}_{j+1} - \Delta\hat{D}_j\right) \\
&= \left(\frac{\upsilon_e}{J}\right)_{j+\frac{1}{2}} (\nabla\xi \bullet \nabla\xi)_{j+\frac{1}{2}} I_m \left[\frac{\partial}{\partial\xi}\left(\Delta\hat{D}\right)\right]_{j+\frac{1}{2}}
\end{aligned}
$$

Eq.(9) can be approximately solved using Gauss-Seidel line relaxation method by transforming the block heptad-diagonal matrix equations into block tri-diagonal matrix equations.

6 Turbulence model

The turbulance model used in this computation is Baldwin-Barth one-equation turbulence model. This turbulence model, derived from a simplified form of the standard $k-\varepsilon$ two equations model, solves one transport

equation for the turbulent Reynolds number $\tilde{R}_T$

$$\frac{D(\upsilon\tilde{R}_T)}{Dt} = (C_{\varepsilon 2} f_2 - C_{\varepsilon 1})\sqrt{\upsilon\tilde{R}_T P} + \left(\upsilon + \frac{\upsilon_t}{\sigma_\varepsilon}\right)\nabla^2(\upsilon\tilde{R}_T) - \frac{1}{\sigma_\varepsilon}(\nabla\upsilon_t)\bullet\nabla(\upsilon\tilde{R}_T)$$

where the eddy viscosity is defined as

$$\upsilon_t = C_\mu(\upsilon\tilde{R}_T)D_1D_2$$

and the damping function D_1 and D_2 are defined as

$$D_1 = 1-\exp\left(-\frac{y^+}{A_0^+}\right) \qquad D_2 = 1-\exp\left(-\frac{y^+}{A_2^+}\right)$$

respectively, and the production term is given by

$$P = \upsilon_t\left(\frac{\partial U_i}{\partial x_j}+\frac{\partial U_j}{\partial x_i}\right)\frac{\partial U_i}{\partial x_j}$$

and f_2 is given by

$$f_2(y^+) = \frac{C_{\varepsilon 1}}{C_{\varepsilon 2}} + \left(1-\frac{C_{\varepsilon 1}}{C_{\varepsilon 2}}\right)\left(\frac{1}{ky^+}+D_1D_2\right) \cdot\left(\sqrt{D_1D_2}+\frac{y^+}{\sqrt{D_1D_2}}\left(\frac{D_2}{A_0^+}\exp\left(-\frac{y^+}{A_0^+}\right)+\frac{D_1}{A_2^+}\exp\left(-\frac{y^+}{A_2^+}\right)\right)\right)$$

The constants used in the model are given by

$$C_{\varepsilon 1}=1.2 \quad C_{\varepsilon 2}=2.0 \quad C_\mu = 0.09 \quad A_0^+ = 26$$

$$A_2^+ = 10 \quad k = 0.41$$

$$\frac{1}{\sigma_\varepsilon} = (C_{\varepsilon 2}-C_{\varepsilon 1})\frac{\sqrt{C_\mu}}{k^2}$$

7 Boundary conditions

At a no-slip surface, the velocity is specified to be zero, and the pressure at the boundary is obtained by specifying that the pressure gradient normal to the wall be zero. The velocity condition for inflow regions is assumed to be the velocity of freestream on the far-field boundaries and the pressure is obtained by extrapolated from the interior domain. The pressure condition for outflow regions is assumed to be the pressure of of freestream on the far-field boundaries and the velocity is obtained by extrapolated from the interior domain.

8 Computational model and computational grid

The birds whose dimension is similar to fixed-wing MAVs can glide freely in the sky, which shows that they possess good aerodynamic performance. By observing their wings, we can find that they are thin and cambered. According to these characters, three class of low-aspect-ratio thin wings (thickness=1.93%) are to be studied for their aerodynamic performance. The airfoil of the first kind wing (W1) is thin and flat; the second airfoil (W2) is thin and semi-cambered, namely, with camber on the half chord near trailing edge and without camber on the half chord near leading edge; and the third airfoil (W3) is thin and cambered. The details of W1 and W3 can be found in Ref.[5]. The shape of the three airfoils can be seen from Figure1 to Figure 3.

Fig.1. Thin Flat Airfoil (W1)

Fig.2 .Thin Semi-cambered Airfoil (W2)

Fig.3 .Thin Cambered Airfoil (W3)

The computational grid was generated using the hyperbolic grid generation method[6], and the topology structure is C-H type with $121\times40\times31$ mesh points, 121 mesh points in the chord direction (81 mesh points on the wall surface) and 40 mesh points in the spanwise direction (26 points on the wall surface).

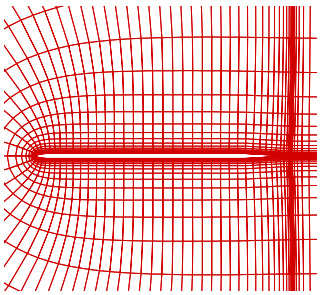

Fig.4. Mesh For Thin Flat Wing

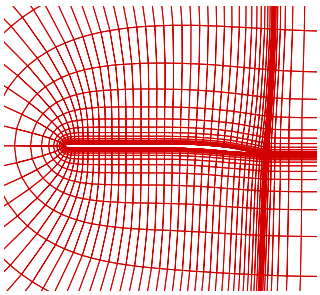

Fig.5. Mesh For Thin Semi-cambered Wing

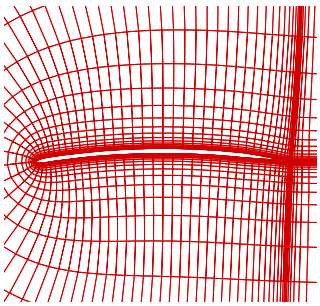

Fig.6 .Mesh For Thin Cambered Wing

It is assumed that the length of the root chord is 15 cm, and the velocity is 15m/s, so the typical value of the cruising Reynolds number is about 140,000. According to the above assumption, the Reynolds number used here is 140,000.

9 Validation

The plots of lift coefficient and drag coefficient versus attack angle are shown from Figure 7 to Figure 10. For the thin flat wing with aspect ratio 1.0, the computational results agree well with the experimental data[5]. A noteworthy achievement is the computational accuracy for drag coefficient which shows that the numerical method is successful. As regard to the computational results of thin cambered wing with aspect ratio 1.0, there is a little departure with the experimental data, the main reason is that the definition of thin cambered wing in the original reference is blurry, and the computational model used here may be different from it.

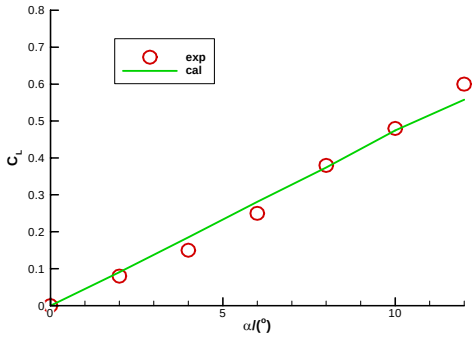

Fig.7.Lift Coefficient Of Thin Flat Wing

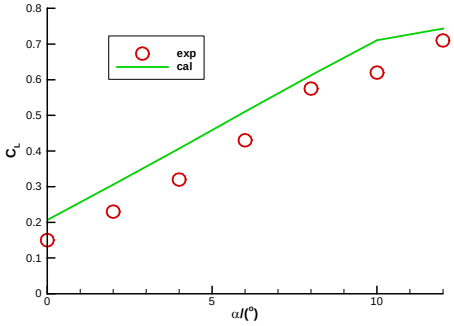

Fig.8 .Lift Coefficient Of Thin Cambered Wing

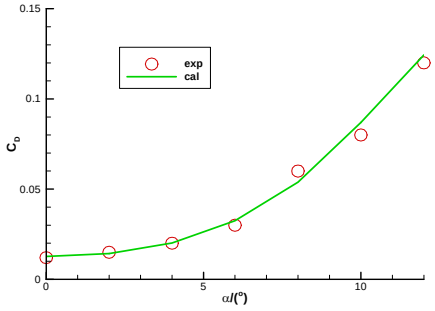

Fig.9.Drag Coefficient Of Thin Flat Wing

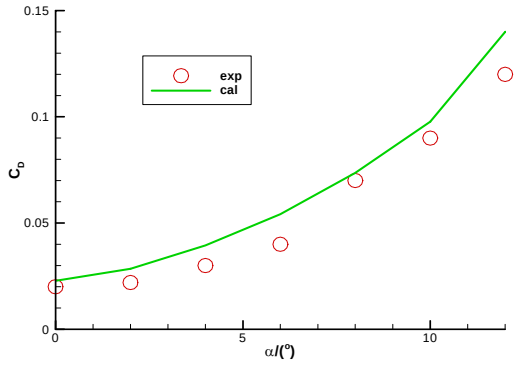

Fig.10. Drag Coefficient Of Thin Cambered Wing

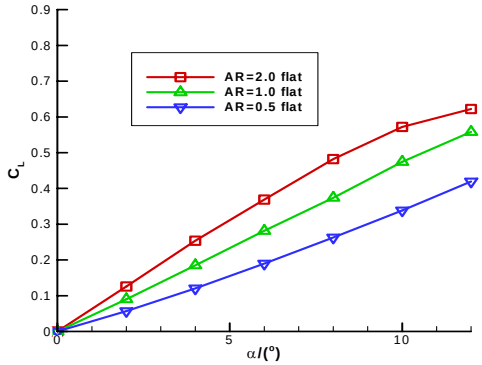

Fig.11. Lift Coefficient Of Thin Flat Wings With Different Aspect Ratio

10 Effects of aspect ratio

Figure 11 to Figure 14 show the lift coefficient curve and the drag coefficient curve of two kinds of wings (W1 and W3, camber=4%) with aspect ratio 0.5, 1 and 2 respectively. It can be obviously seen from these figures that the lift coefficient increases with the increase of aspect ratio and the lift coefficient of thin cambered wing is obviously higher than that of thin flat wing. Tip vortices of the low aspect ratio wing play an important role in the whole flow field. The vortices, similar to leading edge vortices of delta wings, can provide non-linear lift force. From figure 11 and figure 12, we can find that the slope of lift coefficient curve may decrease with the increase of attack angle with aspect ratio 1 and 2, but the slope of lift coefficient curve may be increasing a little with aspect ratio 0.5. The reason is that tip vortices can provide obvious non-linear lift force. This effect will become much more obvious when the attack. angle increases.

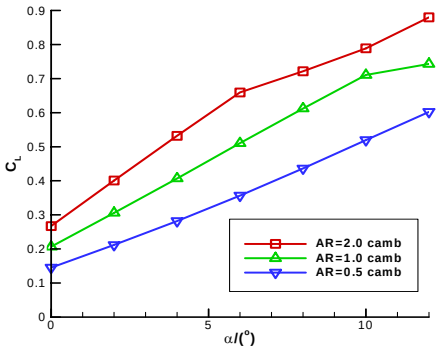

Fig.12. Lift Coefficient Of Thin Camber Wings With Different Aspect Ratio

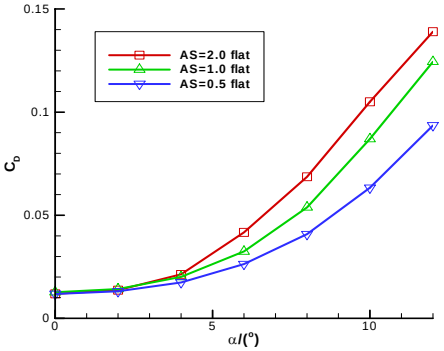

Fig.13. Drag Coefficient Of Thin Flat Wings With Different Aspect Ratio

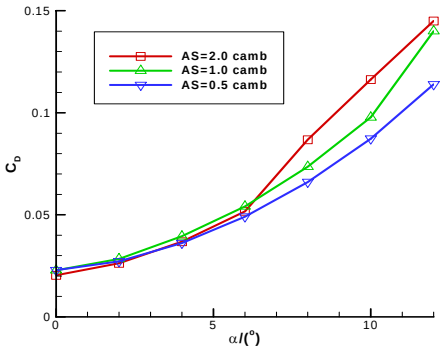

Fig.14. Drag Coefficient Of Thin Camber Wings With Different Aspect Ratio

11 Effects of camber

Figure 15 to Figure 17 illustrate the camber effect on aerodynamic performance. Three wings with the same aspect ratio 1.0 and various camber of 2%, 4% and 6% respectively are studied. From figure15 and figure16, we can find that lift coefficient and drag coefficient are all increasing with the increase of camber. Lift-to-drag ratio curve is plotted in figure17. The corresponding attack angle with maximum lift-to-drag ratio for wings with 4% and 6% camber is 2^o, while that of wing with 2% camber is 4^o. Moreover, the maximum lift-to-drag ratio of the latter is higher than that the former.

When the attack angle is 8^o, the aerodynamic performance of the wing with 4% camber is obviously superior to the other wings. The reason is that it's lift-to-drag ratio is close to that of the wing with 2% camber but it's lift coefficient is much higher than that of the wing with 2% camber. When the attack angle is 10^o, it is the wing with 6% camber. The reason is the same. When the attack angle is 12^o, it is found that the wing with 6% camber has both higher lift-to-drag ratio and higher lift than the others. It's worthy to note that the lift-to-drag ratio of the three kinds of wings are all decreasing with the increase of angle of attack.

The effects of different kinds of camber are given by figure 18 and figure 19. Three wings of the same aspect ration 1.0 with 0% camber (flat), 4% semi-camber and 4% camber are investigated. Although the lift coefficient of semi-cambered wing is slightly higher than that of the camber wing when the attack angle at 0^o~6^o, there is no large difference between the lift coefficients of them for the attack angle within 0^o~10^o. It is worth indicating that there is large difference between the drag coefficients of them, the drag coefficient of semi-cambered wing is obviously larger than that of cambered wing. So, thin semi-cambered wing should be abnegated in the design of MAVS because the aerodynamic performance of thin cambered wing (camber=4%) is superior to that of thin semi-cambered wing.

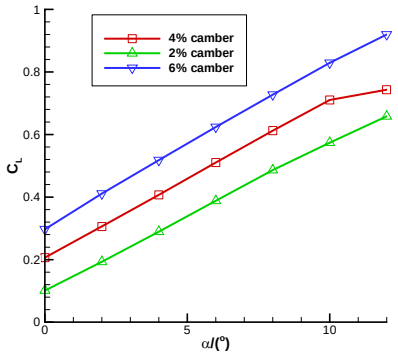

Fig.15. Lift Coefficient Of Thin Wings With Different Camber

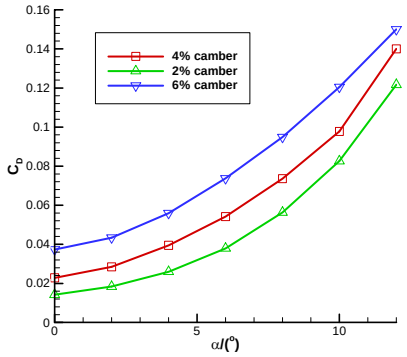

Fig.16. Drag Coefficient Of Thin Wings With Different Camber

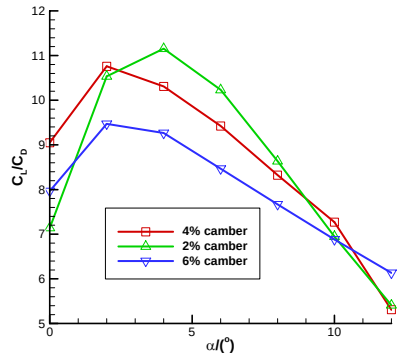

Fig.17. L/D Ratio Of Thin Wings With Different Camber

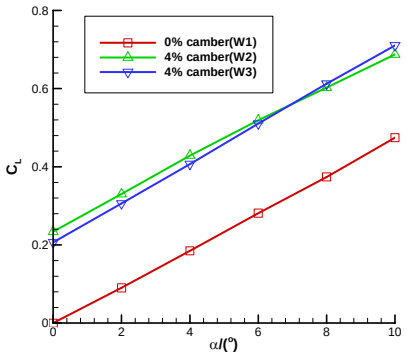

Fig.18. Lift Coefficient Of Three Kinds Of Thin Wings

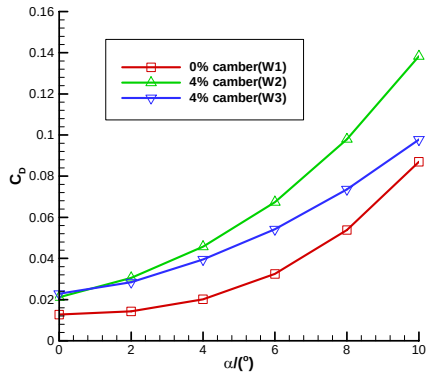

Fig.19. Drag Coefficient Of Three Kinds Of Thin Wings

12 Surface flow structures

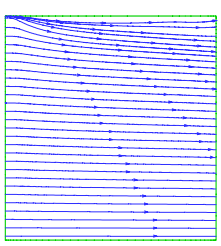

(a) Thin flat airfoil (W1)

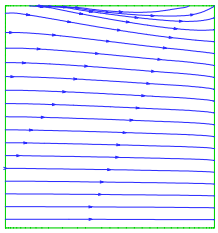

(b) camber=2%(W3)

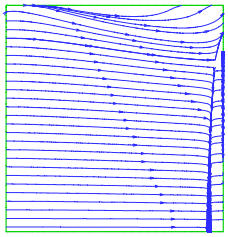

(c) camber=4% (W3)

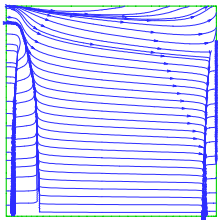

(d)camber=4%(W2)

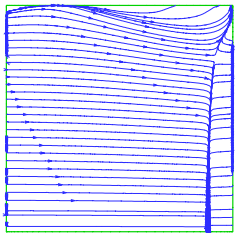

(e) camber=6%(W3)

Fig.20 .Surface Streamline (α =2°， AR=1.0)

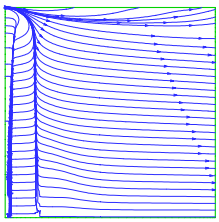

(a) Thin flat airfoil (W1)

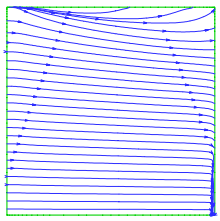

(b) camber=2% (W3)

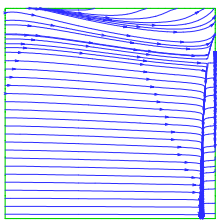

(c) camber=4% (W3)

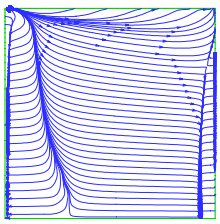

(d) camber=4% (W2)

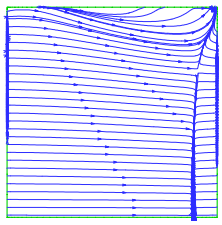

(e) camber=6% (W3)

Fig.21. Surface Streamline (α =4°， AR=1.0)

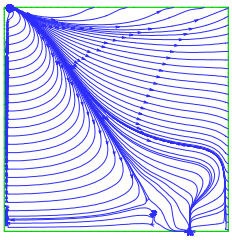

(a) Thin flat airfoil (W1)

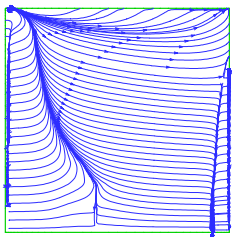

(b)camber=2%(W3)

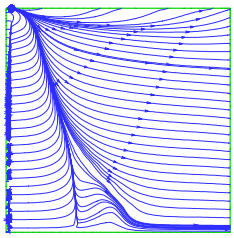

(a) Thin flat airfoil (W1)

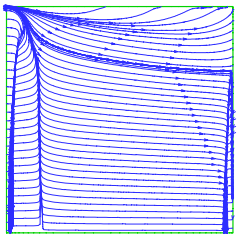

(b) camber=2%(W3)

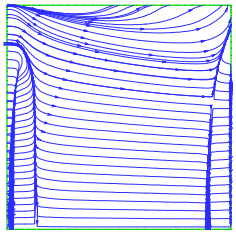

(c) camber=4% (W3)

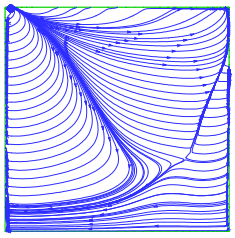

(d) camber=4% (W2)

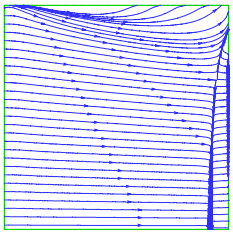

(c) camber=4% (W3)

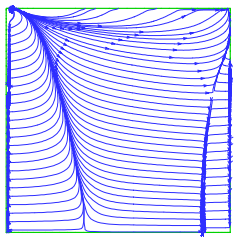

(d) camber=4% (W2)

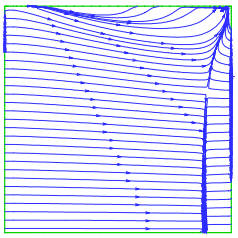

(e) camber=6% (W3)

Fig.22. Surface Streamline (α =6°， AR=1.0)

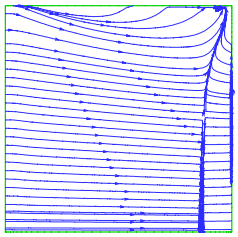

(e) camber=6% (W3)

Fig.23. Surface Streamline (α =8°， AR=1.0)

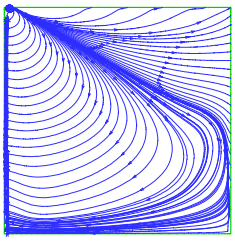

(a) Thin flat airfoil (W1)

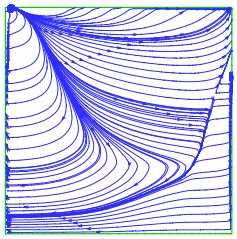

(b) camber=2% (W3)

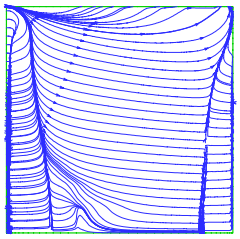

(c) camber=4% (W3)

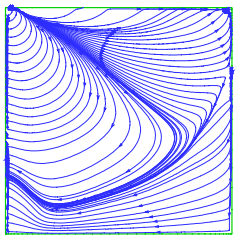

(d) camber=4% (W2)

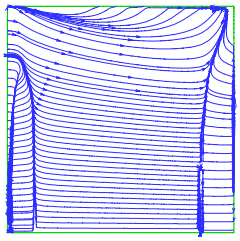

(e) camber=6% (W3)

Fig.24. Surface Streamline (α =10°， AR=1.0)

The upper surface streamlines of various kinds of wings (AR=1) are plotted from figure20 to figure 24.

At 2° attack angle, no separation occur on the upper surface for the flat wing and 2% cambered wing, but it's not true for 4% semi-cambered

cambered wing is much larger due to the higher adverse pressure gradients caused by it's maximum camber.

At 4° attack angle, there is leading separation bubbles on the upper surface for flat wing and semi-cambered wing, but not for the others. Together with the plots for larger attack angle, we can find that the appearance of leading separation bubble can be avoided for a wing with larger leading camber. Even the leading separation bubble occurs for this wing, the separation region is much smaller than that of a wing with small leading camber. In fact, there is adverse pressure gradient in the pressure recovery part along the leading edge. With the low energy carried by the low Reynolds number flows, the kinetic energy within boundary layer is often not strong enough to overcome the adverse pressure gradient, so it's easy to form leading separation bubble. But for a wing with leading camber, the stream tube area decreases along the flow direction, consequently, the average velocity increases and the corresponding pressure decreases along the flow direction. So the extrusion caused by the leading camber will result in the reduction of adverse pressure gradient in the pressure recovery part, which makes the separation region smaller and even no separation. But the extrusion effect will reduce with the increase of attack angle.

At 6° attack angle, there is leading separation bubbles for flat wing, 2% cambered wing and 4% semi-cambered wing, but not for wings with 4% or 6% camber. This phenomenon also shows that the larger leading camber results in small separation, even no separation.

At 8° attack angle, there is leading separation bubble for all wings except the wing with 6% camber. It is observed that no reattachment occurs for flat wing and semi-cambered wing.

At 10° attack angle, there is leading-edge separation bubble for all wings. For flat wing, semi-cambered wing and 2% cambered wing, there is no reattachment near the wing root, but it's not true for 4% and 6% cambered wings. This phenomenon illuminates the extrusion effect on leading separation region once again.

On the all conditions with the appearance of separation bubbles, we can find that the range of separation bubbles becomes larger gradually from wing tip to wing root. The occurrence of this phenomenon may be caused by the strong tip vortex of low-aspect-ratio wings. The tip vortex strengthens the mix of the flow near the tip, which enhances the energy of main flows, and the ability of overcoming the adverse pressure gradient.

13 Conclusions

(1) By comparing the numerical results of thin flat wings (W1) with the experimental results, we can find that the numerical method developed in this article is applicable to simulate the low Reynolds number flows around MAVS wings

(2) The influence of various aspect ratio and camber on the aerodynamic performance of wings was posted by the numerical analysis of low Reynolds number flows around various kinds of low-aspect-ratio wings. The aerodynamic performance of wings become better with the increase of aspect ratio; within the region studied in this article, the lift coefficient and drag coefficient increase with the increase of camber, the numerical computational result shows that wings with 2% camber have the maximum lift-to-drag ratio.

(3) The difference of flow structure of wings with various camber was also posted by analysis of the flow structure of all kinds of wings.

References

[1] Chorin, A. “A numerical method for solving incompressible viscous flow problems,” *Journal of Computational Physics*, vol. 2, No. 1, 1967, pp. 12-26.

[2] Rogers, S. E., Kwak, D. “Steady and unsteady solutions of the incompressible Navier-Stokes equations,” *AIAA Journal*, vol. 29, No. 4, pp. 603-610, 1989.

[3] Rogers, S. E., Kwak, D. “An upwind differencing scheme for the steady-state incompressible Navier-Stokes equations,” NASA TM-101051, 1988.

[4] Baldwin, B. S., Barth, T. J. “A one-equation turbulence transport model for high Reynolds number wall-bounded flows,” NASA TM 102847, 1990.

[5] Pelletier, A., Mueller, T.J.“Low Reynolds number aerodynamics of low-aspect-ratio, thin/flat/cambered-plate wings,” *Journal of Aerialcraft*, vol. 37, No. 5, pp. 825-832, 2001.

[6] Yang, A. M., Weng, P. F. “Hyperbolic Grid Generation Based on Upwind Schemes,” *Acta Aerodynamica Sinica*, vol. 22, No.01, 2004.

[7] Mueller,T.J., DeLaurier, J. D. “Aerodynamics of small vehicles,” *Annual Review of Fluid Mechanics*, vol. 35, pp. 89-111, 2003